First-principles simulations of the porous layered calcogenides Li_{2+x}SnO_{3} and Li_{2+x}SnS_{3}

Jason Howard and N. A. W. Holzwarth

First principles simulations of the porous layered calcogenides $\mathrm{Li_{2+x}SnO_3}$ and $\mathrm{Li_{2+x}SnS_3}$

Jason Howard and N. A. W. Holzwarth[*]

Department of Physics, Wake Forest University, Winston-Salem, NC 27109-7507 USA

(Dated: August 2, 2016)

First principles simulations of the porous layered calcogenide materials $\mathrm{Li_2SnO_3}$ and $\mathrm{Li_2SnS_3}$ are used to study their structures, Li ion mobilities, and their interactions with excess Li. The pristine materials are characterized by a regular pattern of voids within the calcogenide layers which are occupied by intralayer Li ions. The energetically most favorable Li ion migration processes for both materials result in a net motion perpendicular to the layers and involve intralayer Li ions and nearby interstitial sites. The ideal lattice has 8 symmetry related stable interstitial sites within the conventional unit cell which, in addition to participating in the Li ion migration processes, are also important for accomodating excess Li during lithiation processes. Consistent with experimental findings, the simulations find that the addition of Li atoms to $\mathrm{Li_2SnO_3}$ results in a disruption of the calcogen lattice with the breaking of Sn-O bonds. The estimated voltage versus bcc Li for this system is in qualitative agreement with experiment provided that Sn/Li disorder is taken into account. By contrast, the simulations predict that the addition of Li atoms to $\mathrm{Li_2SnS_3}$ results in a stable metallic material up to a stoichiometry of $\mathrm{Li_3SnS_3}$. This prediction has not yet been studied experimentally. Simulations of surfaces of these materials find that it is energetical favorable to add a small amount of excess surface Li. However, interfaces of these materials with Li metal are found to be reactive. Some of the findings may be relevant to other materials having the same crystal structure such as $\mathrm{Li_2MnO_3}$ and $\mathrm{Li_2TiO_3}$.

I. INTRODUCTION

Efficient ionic conductivity in crystalline materials depends on a delicate balance of structural, chemical bonding, and charge transfer factors. The study of Li ion conduction in $\mathrm{Li_2SnO_3}$ and $\mathrm{Li_2SnS_3}$ provides an interesting example of these factors with possible implications for a variety of technologies including solid state batteries.

The crystal structure of $\mathrm{Li_2SnO_3}$ and $\mathrm{Li_2SnS_3}$ is related to the structure of layered dichalcogenides such as $\mathrm{SnS_2}$.[1] A patterned layer of the calcogenide is constructed by systematically removing one-third of the Sn atoms within a layer of $\mathrm{SnS_2}$, leaving star-shaped voids. Filling these voids with Li, results in a structure similar to the corresponding layers in $\mathrm{Li_2SnO_3}$ and $\mathrm{Li_2SnS_3}$, as shown in Fig. 1. In $\mathrm{SnS_2}$ each calcogen is bonded to three Sn atoms, while the void pattern in $\mathrm{Li_2Sn(O/S)_3}$ allows for each calcogen to be bonded to two Sn atoms. As will be discussed in more detail in Sec. III, the full structure of $\mathrm{Li_2Sn(O/S)_3}$ includes a particular stacking of the layers and the placement of interlayer Li sites.[2–4] Interestingly, a number of other Li ion conducting materials have the this same structure including $\mathrm{Li_2MnO_3}$ and $\mathrm{Li_2TiO_3}$.[5,6]

The conductivity of Li ions in $\mathrm{Li_2SnO_3}$ has been measured to be very small (10^{-8} S/cm at 290° C), although the activation barrier for conduction is in a reasonable range.[7] One of the interesting proposed uses for $\mathrm{Li_2SnO_3}$ is as an anode material for lithium ion batteries.[8–10] The mechanism involves the material undergoing an irreversible decomposition during the first lithiation of the material forming a composite of $\mathrm{Li_2O}$ and $\mathrm{Li_xSn}$. $\mathrm{Li_2O}$ serves to buffer the volume expansion of the active anode material $\mathrm{Li_xSn}$. $\mathrm{Li_2SnO_3}$ is among other tin based electode materials with a similar mechanism such as $\mathrm{SnS_2}$, SnO, and $\mathrm{SnO_2}$.[8,11,12] By contrast, Brant *et al.*[4] showed
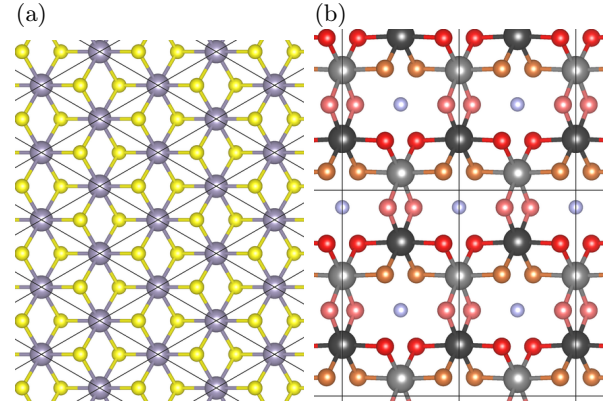

FIG. 1. (Color online.) (a) Planar projection of ball and stick model of a single layer of $\mathrm{SnS_2}$ with grey and yellow balls representing Sn and S, respectively. Lines indicate the two-dimensional (hexagonal) unit cells. (b) Planar projection of ball and stick model of a single layer of $\mathrm{Li_2SnO_3}$, excluding the interlayer Li sites. This structure has two inequivalent Sn sites indicated with two shades of grey, three inequivalent O sites indicated with three shades of red, orange, and pink, and one Li inequivalent intralayer Li site indicated with light blue. Lines indicate the boundaries of the two-dimensional unit cells.

that $\mathrm{Li_2SnS_3}$ has good ionic conductivity (10^{-5} S/cm at 25° C). The lithiation properties of $\mathrm{Li_2SnS_3}$ have not yet been studied.

The purpose of the present study is to computationally examine both $\mathrm{Li_2SnO_3}$ and $\mathrm{Li_2SnS_3}$ in order to understand the mechanisms for Li ion migration, the lithiation processes, and the interface properties. The remainder of the paper is organized as follows. Section II details the computational methods used in this work. Structural details are presented in Sec. III while Li ion migration in

the stoichiometric materials are presented in Sec. IV. Models of the lithiation processes are presented in Sec. V and interfaces with vacuum and with Li metal are discussed in Sec. VI. Section VII contains the discussion and conclusions. Some of the structural details are given in the Appendix.

II. METHODS

The computational methods used in this work were based on density functional theory[13,14] implemented with the projector augmented wave formalism (PAW).[15] The PAW atomic data-sets were calculated using the ATOMPAW code[16] and the materials simulations were performed using the QUANTUM ESPRESSO software package.[17] The local density approximation exchange correlation functional(LDA)[18,19] was used throughout all calculations. The minimum energy path for Li ion migration was estimated using the "nudged elastic band" (NEB) method[20–22] as programmed in the QUANTUM ESPRESSO package, using 5 images between each metastable configuration. In modelling charged defects (Li ion vacancies or interstitials), the system was assumed to remain electrically insulating and a uniform background charge was added in order to evaluate the electrostatic interactions. The partial density of states $\langle N^a(E) \rangle$ were calculated as described in previous work,[23,24] using weighting factors based on the charge within the augmentation spheres of each atom with radii $r_c^{Li} = 1.6$, $r_c^{Sn} = 2.3$, $r_c^{O} = 1.2$, and $r_c^{S} = 1.7$ in bohr units. The reported $\langle N^a(E) \rangle$ curves are averaged over all sites of type a. The isosurfaces of electron density were computed using the PWPAW code[25] and visualized using OpenDX.[26] Structural visualizations used the XcrySDen code[27,28] and the VESTA code.[29]

Integrals over the Brillouin zone used a Gaussian smearing factor of 0.001 Ry and a uniform grid of $4 \times 2 \times 2$ Bloch vectors $\mathbf{k}$ for the conventional unit cells. Supercell simulations used consistent $\mathbf{k}$-point sampling. For evaluating the partial densities of states, the $\mathbf{k}$-point sampling was increased by a factor of 2 in each dimension. The plane wave expansions of the electron wavefunctions included reciprocal lattice vectors $\mathbf{G}$ such that $|\mathbf{k} + \mathbf{G}|^2 \leq 64$ bohr^{-2}. Most of the defect studies were modeled using $2 \times 1 \times 1$ supercells. Spot checks of finite size errors show them to be approximately 0.02 eV for the NEB calculations and for the relative energies of point defects.

III. STRUCTURE

The crystal structures of Li_2SnO_3[2] and Li_2SnS_3[4] are very similar, both having the centered monoclinic space group C2/c (No. 15 as listed in the International Table of Crystallography[30]). The materials are layered in the a-b planes with an A-B stacking sequence. The A and B
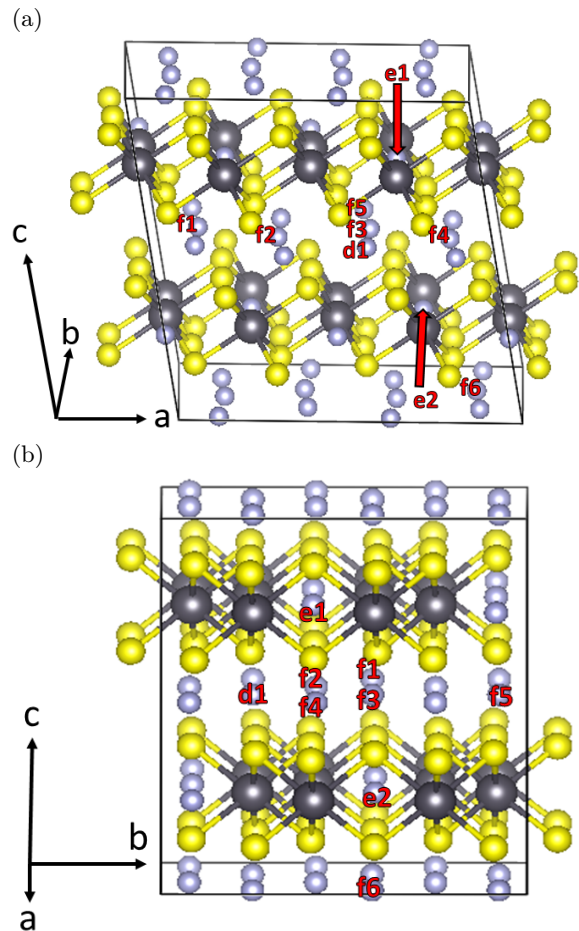

FIG. 2. (Color online) Ball and stick model of Li_2SnS_3 with lithium light grey, tin dark grey, and sulfur yellow. Site labels d_i, f_i, and e_i reference possible lithium vacancy conduction pathways with the letter being the Wyckoff label. Figures (a) and (b) show different viewpoints as labeled by the corresponding axes to the left. This figure is geometrically representative of Li_2SnO_3 as well.

layers are geometrical equivalent but differ by an inversion. Visualizations of the structure are shown in Fig. 2 from two different perspectives. The layered structure of Li_2SnS_3 was described by Kuhn et al.[3] as $Li[Li_{\frac{1}{3}}Sn_{\frac{2}{3}}S_2]$, with the outer Li representing the planes of Li and the inner bracket representing the layers of the complex of tin sulfide plus Li. Using this same notation Li_2SnO_3 can be described as $Li[Li_{\frac{1}{3}}Sn_{\frac{2}{3}}O_2]$.

The crystal axes and angle are labeled a, b, c, and β. Computational and experimental results for lattice parameters are listed in Table I. When scaled by 1.02 to compensate for the systematic LDA lattice contraction, the calculated results agree well with the experimental measurements. The fractional coordinates for the structures are presented in the Appendix A. The electronic structures including band structures and densities of states were previously reported.[4]

In preparation for studying Li ion conduction and lithi-

TABLE I. Computational and experimental lattice parameters for Li_2SnO_3 and Li_2SnS_3. Experimental results for Li_2SnO_3 and Li_2SnS_3 are from Refs. 31 and 4, respectively.

Lattice(Å,°)		Comp.	Exp.
Li_2SnO_3	a	5.22	5.3033(2)
	b	9.06	9.1738(3)
	c	9.78	10.0195(2)
	β	100.31°	100.042(2)°
Li_2SnS_3	a	6.30	6.3964(5)
	b	10.91	11.0864(9)
	c	12.15	12.405(1)
	β	99.94°	99.867(5)°

TABLE II. Relative energies (in eV) of lithium ion vacancies with the zero of energy set to the lowest energy vacancy for each material calculated in a $2\times1\times1$ supercell. The site labels refer to the Wyckoff letters for the distinct Li sites.

Material	d-site	f-site	e-site
Li_2SnO_3	0.11	0.09	0
Li_2SnS_3	0	0	0.35

ation in these materials, the energies of relaxed ideal point defects in $2\times1\times1$ supercells were studied. Table II lists the relative energies of the inequivalent Li ion vacancies. It is of interest to note that the most favorable vacancy in Li_2SnO_3 is located at an e-site while in Li_2SnS_3 the e-site is the location of the least energetically favorable vacancy. Interstitial defects were also studied. In a search of the void regions of the crystal, only one unique site for a stable interstitial defect was found in each material. Within the conventional cells, the interstitial sites have multiplicity and Wyckoff label 8f and are located at the fractional coordinates (0.066, 0.093, 0.425) and (0.062, 0.086, 0.430) for Li_2SnO_3 and Li_2SnS_3, respectively. In both materials, the interstitial sites are located near the Li e-sites of the host lattice, displaced along the c-axis above and below the $[Li_{\frac{1}{3}}Sn_{\frac{2}{3}}(O/S)_2]$ layers.

The literature has identified several other defects in both materials.[3,4,31,32] These defects include Li/Sn antisites and stacking faults. These defects can be important factors in both Li ion migration and lithiation processes.

IV. ION-MIGRATION

Li ion conductivity has been experimentally measured for stoichiometric Li_2SnO_3 and Li_2SnS_3.[4,7] The conductivity can be modeled by an Arrhenius relationship in the form of Eq.(1).

$$\sigma = \frac{A}{T}e^{-E_a/kT} \qquad (1)$$

In this equation A is a constant, T the temperature in Kelvin, k the Boltzmann constant, and E_a the activation energy for Li ion conduction. The activation energy E_a is a parameter that is determined experimentally by analyzing the temperature dependence of the conductivity and can be theoretically approximated through Eq.(2).

$$E_m \leq E_a \leq E_m + \frac{E_f}{2} \qquad (2)$$

The migration energy E_m is the lowest energy barrier for Li ion conduction approximated using NEB calculations. The formation energy E_f is the energy of creating a vacancy interstitial pair calculated using Eq.(3), with E_{defect} and $E_{perfect}$ being total density functional energies in equivalent supercells of the structurally relaxed vacancy interstitial pair and the perfect crystal respectively.

$$E_f = E_{defect} - E_{perfect} \qquad (3)$$

In Eq.(2) the lower limit represents the "intrinsic" case where the material has a large population of native vacancy interstitial defects and the upper limit represents the "extrinsic" case where material has few native vacancy interstitial defects.[33] Additionally, real materials can have other defects such as Li/Sn antisite defects and stacking faults which can be detected by X-ray analysis. For the case of Li_2SnO_3, several samples were studied by Teo et al.[7]. The sample with the lowest E_a and highest conductivity had the sharpest and most complete diffraction peaks. This indicates that this sample is relatively free of these Sn/Li antisite and stacking fault defects.[31]

In computationally determining E_m for the vacancy mechanism, suitable pathways were chosen along the main axes of the $2\times1\times1$ supercell. Two pathways corresponded to migration in the a-b plane in the Li layers between the main $[Li_{\frac{1}{3}}Sn_{\frac{2}{3}}(O/S)_2]$ layers of the material, while the other was a spiral along the c-axis through the $[Li_{\frac{1}{3}}Sn_{\frac{2}{3}}(O/S)_2]$ layers. Geometrically identical pathways were investigated in the two materials using the vacancy labels shown in Fig. 2. The paths in the figure are labeled by their Wyckoff label and numeric identifier. Table II gives the relative energies for the vacancies on the Li site types. The results for the NEB calculations showing the energy landscape connecting the images for the relaxed vacancy configurations are displayed in Fig. 3. The desired quantity from these plots is E_m and it is found by searching for the path with the lowest energy difference between highest and lowest energy along the path. The results for vacancy migration in Li_2SnS_3 are relatively large with migration barriers of $0.6-0.7$ eV for all of the paths. By contrast Li_2SnO_3 shows an interesting result of having $E_m = 0.3$ eV along the c-axis while the other paths have $E_m = 0.8-0.9$eV.

In this study, no viable pure interstitial conduction mechanisms were found. On the other hand several viable interstitialcy[34] mechanisms were found; the most favorable path is shown in Fig. 4. An interstitialcy mechanism
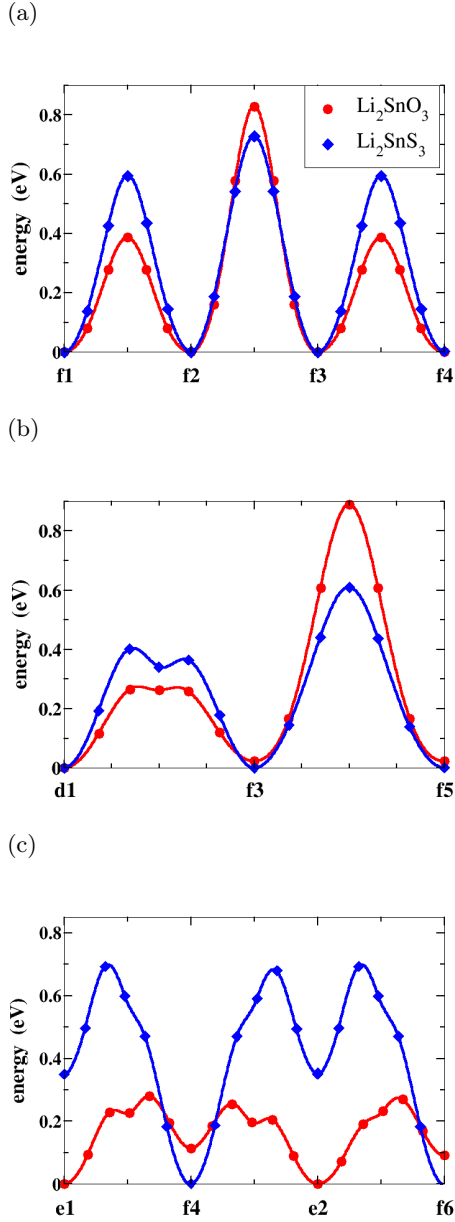
(a)

(b)

(c)

FIG. 3. (Color online) Energy path diagrams for vacancy migration calculated using NEB with Li$_2$SnO$_3$ red and Li$_2$SnS$_3$ blue. Path labels refer to the site labels in Fig.2. The zero of energy for each curve has been set to the lowest energy of that path. Migrations along the a, b, and c axes are shown in plots (a), (b), and (c) respectively.

is one in which an interstitial ion moves into a host lattice site as that host lattice ion moves to an adjacent interstitial location. In Fig. 4 the two unique steps of the path are labeled as "a" and "b" and shown from two viewpoints. In the "a"-step, an interstitial ion moves onto a host e-site as that e-site ion moves to the neighboring interstitial site. In the "b"-step, the interstitial ion moves to the nearest host d-site as that d-site ion moves to the nearest interstitial site. It is the "a"-step that allows the

(a)

(b)
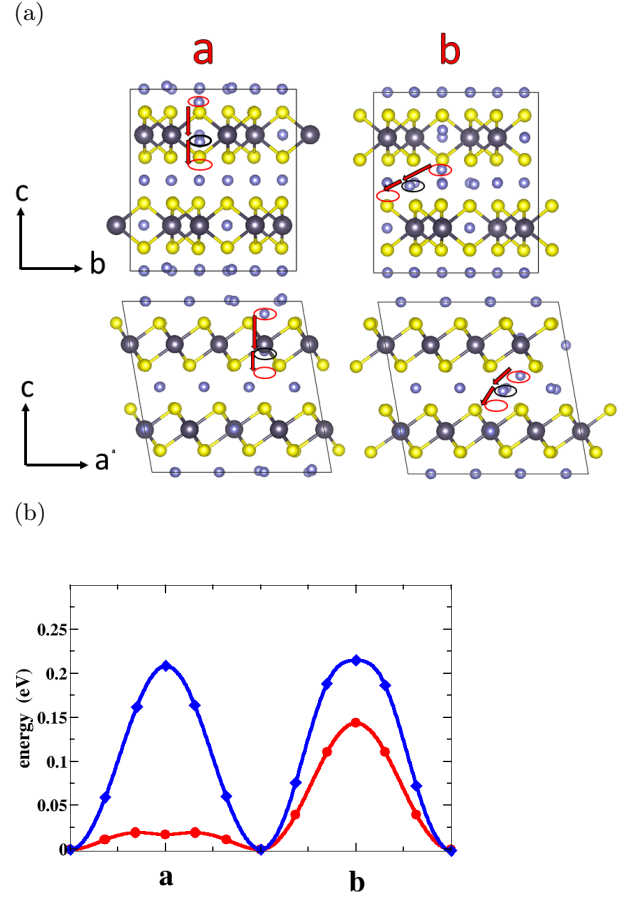
FIG. 4. (Color online) (a) Ball and stick model for the interstitialcy Li ion conduction mechanism in Li$_2$SnS$_3$ using the same ball conventions as in Fig. 2. This figure is geometrically representative for the same conduction mechanism in Li$_2$SnO$_3$. (b) Energy path diagrams for interstitalcy Li ion migration using red for Li$_2$SnO$_3$ and blue for Li$_2$SnS$_3$. The labels a and b above the diagrams in Fig. (a) and the path labels in Fig. (b) refer to the two unique steps of this interstitialcy mechanism.

Li ion to move through the [Li$_{\frac{1}{3}}$Sn$_{\frac{2}{3}}$(O/S)$_2$] layers. The results for the NEB calculations in Fig. 4 show that for both Li$_2$SnO$_3$ and Li$_2$SnS$_3$, this interstitialcy mechanism is the most favorable mode of Li ion conduction. The E_m values for this most favorable interstitialcy mechanism is 0.14 eV for Li$_2$SnO$_3$ and 0.22 eV for Li$_2$SnS$_3$. Interestingly the "a"-step in this process has a markedly smaller barrier than the "b"-step for Li$_2$SnO$_3$, while for Li$_2$SnS$_3$ both steps have approximately the same barrier. The other less favorable interstitialcy mechanisms had E_m values of 0.46 eV for Li$_2$SnO$_3$ and 0.59 eV for Li$_2$SnS$_3$. These mechanisms had equivalent "a"-steps as in Fig. 4 but the "b"-step was different by the involvement of host f-site ions moving to neighboring interstitial sites.

To compare the most favorable E_m for the vacancy and interstitialcy mechanisms with experiment, the inequal-

ity in Eq.(2) is used. To estimate the interstitial-vacancy pair formation energy E_f, Eq. (3) is used. E_{defect} is determined from metastable configurations of a host lattice Li ions displaced into an interstitial site. From these results, the lowest E_f for a vacancy interstitial pair was 1.25 eV for Li_2SnO_3 and 0.96 eV for Li_2SnS_3. If a large population of defects is present in the material, it is expected for E_a to be closer to E_m, while if very few are present E_a is expected to be closer to $E_m + \frac{E_f}{2}$. The results are listed in Table III. The experimental values of E_a for both samples are best explained by the interstitialcy mechanism using the upper limits of Eq. (2). This infers that these samples have a small number of native vacancy-interstitial defects.

TABLE III. Calculated lower an upper bound for E_a from Eq.(2) using the most favorable E_m for the vacancy and interstitialcy mechanisms along the indicated axis. Listed experimental results are from Refs. 7 and 4 respectively. All energies given in eV.

Li_2SnO_3	E_m	E_a	$E_m + \frac{E_f}{2}$
vacancy (c axis)	0.28	$\leq E_a \leq$	0.91
interstitialcy (c axis)	0.14	$\leq E_a \leq$	0.77
experiment		0.69-0.91	
Li_2SnS_3	E_m	E_a	$E_m + \frac{E_f}{2}$
vacancy (b axis)	0.61	$\leq E_a \leq$	1.07
interstitialcy (c axis)	0.22	$\leq E_a \leq$	0.68
experiment		0.59	

V. LITHIATION

A. Geometrical structures

Several authors have studied lithiation of Li_2SnO_3[8–10] and have shown lithium can be absorbed into the material. Experimental lithiation of Li_2SnS_3 has not been reported in the literature. In order to model a possible mechanism of the lithiation for Li_2SnO_3 and Li_2SnS_3, a bulk intercalation process was assumed. This process involved placing excess lithium in the lattice of interstitials given by the coordinates in the Sec. III. There are 8 interstitial sites per conventional cell.

Initially a random sampling of configurations of lithium placed in the interstitial sites for $2\times1\times1$ supercells were optimized with full structural relaxations for $0 \leq x \leq 1$ in $Li_{2+x}Sn(O/S)_3$. The limit $x = 1$ corresponds to filling all available interstitial sites defined for the perfect lattice. A sample of these configurations over the concentration range is shown in Fig. 5. It is shown in Fig. 5(a) that $Li_{2+x}SnO_3$ gradually becomes disor-
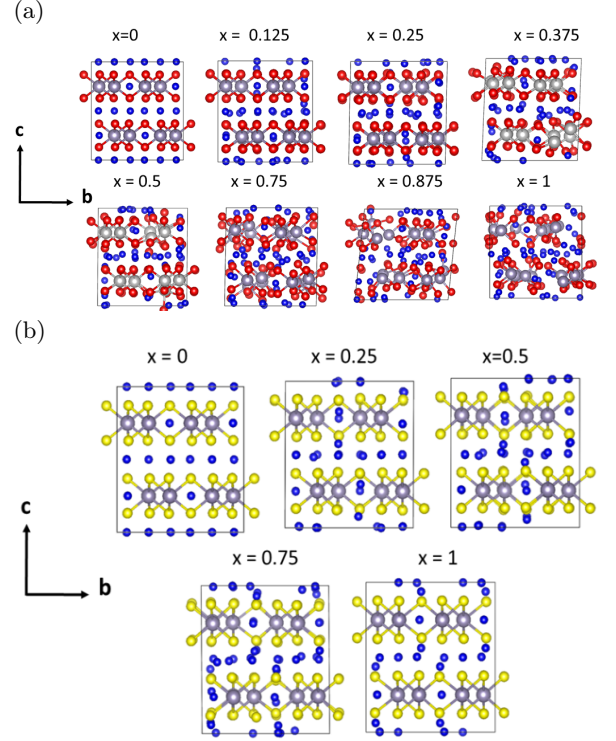

FIG. 5. (Color online) Ball and stick models of optimized structures for $Li_{2+x}SnO_3$ in (a) and $Li_{2+x}SnS_3$ in (b) for indicated values of x. Li, Sn, O, and S are represented by blue, gray, red, and yellow balls respectively.

dered as x increases. Qualitatively the material could be described as experiencing an amorphous transition at $x \approx 0.75$, which is consistent with the findings of Zhang et al.[9] who show that $Li_{2+x}SnO_3$ loses its diffraction peaks in the range $0.75 \lesssim x \lesssim 5$. Figure 5(b) shows that the computed model of $Li_{2+x}SnS_3$ is stable up to $x = 1$. Analysis of the change in cell parameters are given in the Appendix B . The lattice of $Li_{2+x}SnO_3$ expands monotonically with concentration along all axes for $0 \leq x < 0.5$. For $0.5 \leq x \leq 1$ the expansion continues to be monotonic but there is a large variability in the cell parameters. The lattice of $Li_{2+x}SnS_3$ expands monotonically across all axes for $0 \leq x \leq 1$ with relatively small variability in the results due to Li configurations.

B. Electronic structures

Partial density of states calculations in the range $0 \leq x \leq 1$ are shown in Figs. 6 and 8. The partial density of states for $x = 0$ for both materials agree with those presented by Brant et al..[4] While the calculational methods are known to underestimate the energies of the band gaps, the relative energies are expected to be well represented.

Pristine Li_2SnO_3 is found to have a relatively large band gap (roughly 4 eV). For $x > 0$, an occupied
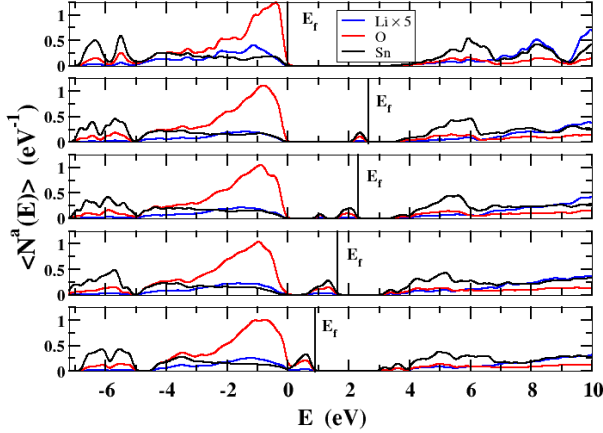
FIG. 6. (Color online) Partial density of states for $Li_{2+x}SnO_3$ with the zero of energy set to top of the occupied valence band of the pure material. In addition to the partial density of states for the perfect crystal, a sample of results for $x = 0.25, 0.5, 0.75$ and 1.0, calculated within the $2\times1\times1$ supercell, are presented in separate panels. For visibility, the lithium curves were scaled by a factor of 5.

FIG. 7. (Color online.) Ball and stick diagram of an orthorhombic section of a unit cell of $Li_{2.25}SnO_3$ with Li, Sn, and O indicated with blue, grey, and red balls, respectively. Isosurfaces bounding the $0.1e/Å^3$ density level of the states associated with the excess electrons are indicated in green. The orientation is similar to that of Fig. 2(b).

impurity-like band appears within the original band gap for $Li_{2+x}SnO_3$. The impurity band moves towards the top of the valence as x increases, as shown in Fig. 6.

In order to get a better idea of the nature of the "gap states" in $Li_{2+x}SnO_3$, an example of a $x = 0.25$ configuration within the conventional cell was modeled and the results are shown in Fig. 7. Isosurfaces of the electron density associated with the occupied intercalation states are shown. In this case, the intercalation density is localized primarily on O sites near one of the Sn sites which has a broken Sn-O bond.

By contrast, pristine Li_2SnS_3 is found to have a small band gap (roughly 1 eV), due to unoccupied conduction bands formed from the hybridization of Sn $5s$ and S $3p$ orbitals. For $x > 0$, the excess electrons of $Li_{2+x}SnS_3$ occupy the available conduction states with little change in the shapes of the partial densities of states curves, as shown in Fig. 8.

Figure 9 illustrates the isosurfaces for the excess electron charge density in $Li_{2+x}SnS_3$ for two selected configurations at $x = 0.5$ and $x = 1.0$ in the conventional cell. The form of the isosurfaces is consistent with an antibonding hybridization of the Sn $5s$ and S $3p$ states that make up the conduction band. In the $x = 1$ case the isosurfaces for the two layers are related by an inversion consistent with the symmetry of the lattice.
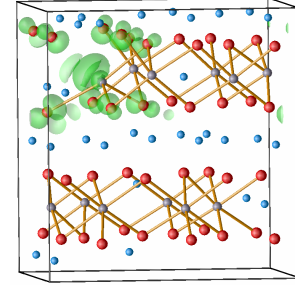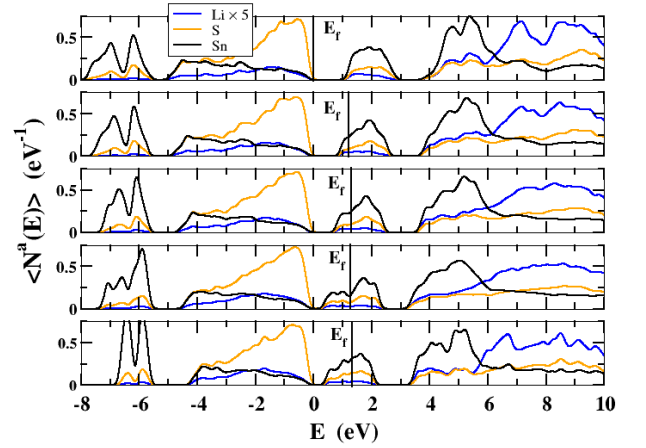

FIG. 8. (Color online) Partial density of states for $Li_{2+x}SnS_3$ with the zero of energy set to the top of the occupied valence band of the pure material. In addition to the partial density of states for the perfect crystal, a sample of results for $x = 0.25, 0.5, 0.75$ and 1.0, calculated within the $2\times1\times1$ supercell, are presented in separate panels. For visibility, the lithium curves were scaled by a factor of 5.

C. Voltage profiles

The average open cell voltage of the compound $Li_{2+x}Sn(O/S)_3$ lithiated with x Li ions per formula unit versus bcc lithium metal can be approximated by[35]

$$V_{avg}(x) = \frac{-\Delta E}{x} = \frac{\int_0^x dx' V_{obs}(x')}{x}. \qquad (4)$$

For computational reasons, it is convenient to calculate the averaged voltage between the two intercalation limits $Li_{2+x}Sn(O/S)_3$ and $Li_2Sn(O/S)_3$ and Eq. (4) can be used to relate the result to an experimental voltage $V_{obs}(x)$. The approximation assumes that the internal energy difference ΔE is a good approximation to the Gibbs free
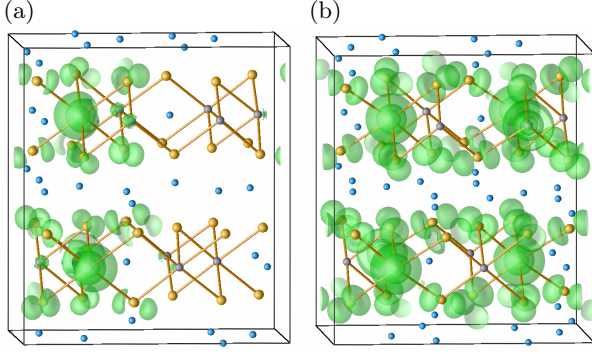
FIG. 9. (Color online.) Ball and stick diagrams of an orthorhombic sections of unit cells of $Li_{2.5}SnS_3$ (a) and Li_3SnS_3 (b), with Li, Sn, and S indicated with blue, grey, and yellow balls, respectively. Isosurfaces bounding the $0.03e/Å^3$ density level of the states associated with the excess electrons are indicated in green. The orientation is similar to that of Fig. 2(b).

energy difference ΔG where $\Delta G = \Delta E + P\Delta V - T\Delta S$. This implies that $P\Delta V$ and $T\Delta S$ as small compared with ΔE. We further approximate ΔE by its value at $T = 0$ K.

In practice, for a given value of x there are many possible configurations (σ) of the lithium interstitials. Each of these configurations will have a configuration dependent internal energy difference $\Delta E_\sigma(x)$ given by

$$\Delta E_\sigma(x) = E^\sigma_{Li_{2+x}Sn(O/S)_3} - E_{Li_2Sn(O/S)_3} - xE_{Li_{bcc}}. \quad (5)$$

The internal energy difference of the system can be determined by averaging over all of the configurations

$$\Delta E(x) = \sum_\sigma \Delta E_\sigma(x)P_\sigma(x), \quad (6)$$

where $P_\sigma(x)$ denotes the probabilty of any given configuration σ at Li concentration x.

Open cell voltages are an equilibrium process so the probabilities can be approximated by a Boltzmann distribution at temperature T:

$$P_\sigma(x) = \frac{e^{-\Delta E_\sigma(x)/kT}}{Z(x)} \quad \text{where} \quad Z(x) = \sum_\sigma e^{-\Delta E_\sigma(x)/kT}. \quad (7)$$

Here k denotes the Boltzmann constant and $Z(x)$ denotes the partition function. In practice, it is difficult to sample enough configurations to evaluate the probabilities in Eq. (7) using first principles alone. However, qualitative information is readily available from samples of the configuration and concentration dependent voltages $V_\sigma(x)$ defined as

$$V_\sigma(x) = -\frac{\Delta E_\sigma(x)}{x}, \quad (8)$$

and presented in Figs. 10 and 11. In Fig. 10, the simulations were done using $2 \times 1 \times 1$ supercells. For each

concentration x with $0.0625 < x < 1$, two randomly chosen configurations σ were computed. For $x = 0.0625$ and $x = 1$ only one unique configuration is possible for these supercells. Figure 11, includes results from a variety of supercells. The results for $0.0625 < x \leq 0.5$ all had their initial configurations chosen randomly aside from the special case of $V_\sigma(x = 0.25) = 0.53$ V.
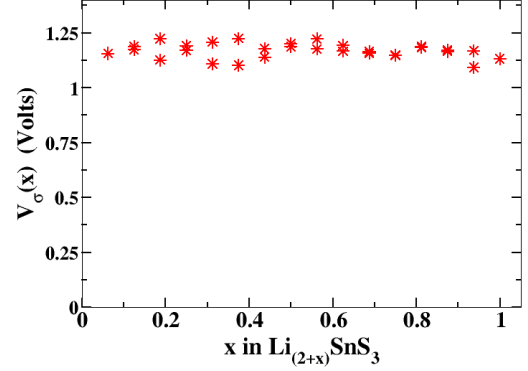

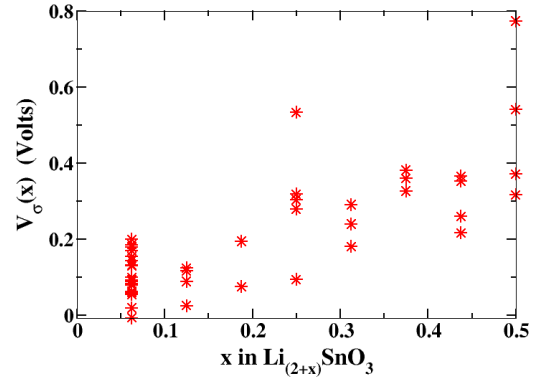FIG. 10. Sampling of $V_\sigma(x)$ calculated with Eq. (8) for $Li_{2+x}SnS_3$.

FIG. 11. Sampling of $V_\sigma(x)$ calculated with Eq. (8) for $Li_{2+x}SnO_3$.

Due to its stable interstitial lattice, to interpret the results for $Li_{2+x}SnS_3$, the ideas of cluster expansion[36] can be used. The idea of a cluster expansion is to expand $\Delta E_\sigma(x)$ over a set of configuration variables $\sigma_i..\sigma_k$ and effective cluster interactions $E_{i..k}$ as in Eq. (9).

$$\Delta E_\sigma(x) = \sum_i E_i\sigma_i + \sum_{i,j} E_{ij}\sigma_i\sigma_j + \sum_{i,j,k} E_{ijk}\sigma_i\sigma_j\sigma_k.... \quad (9)$$

The E_i, E_{ij}, and E_{ijk} ... terms represent the lattice site, pairwise interaction, and three site interactions, respectively. For this system, the E_i terms are all equivalent

due to the interstitial sites being geometrically equivalent. If the E_i terms are concentration independent and if higher order terms $E_{i..k}$ are small, then $\Delta E_{\boldsymbol{\sigma}}(x)$ can be approximated by Eq. (10).

$$\Delta E_{\boldsymbol{\sigma}}(x) \approx \sum_i E_i \sigma_i \propto x E_i \qquad (10)$$

This implies that a plot of $V_{\boldsymbol{\sigma}}(x)$ will be approximately constant over x and $\boldsymbol{\sigma}$. The plot in Fig. 10 shows this behavior so we can infer that in $\mathrm{Li}_{2+x}\mathrm{SnS}_3$ the lattice site interaction is concentration independent and is large compared to the pairwise and higher interactions. For this constant voltage case, we can predict that the measured voltage will be $V_{obs}(x) \approx 1.2$ V.

While there has apparently not yet been an experimental measurement of the intercalation voltage of $\mathrm{Li}_{2+x}\mathrm{SnS}_3$, there have been several measurements of the intercalalation voltage of $\mathrm{Li}_{2+x}\mathrm{SnO}_3$ reported in the literature.[8–10] The literature results find $V_{obs}(x)$ to be a *decreasing* function of x with $V_{obs}(x)$ varying from ~ 1.0 V to ~ 0.4 V for $0 \leq x \leq 0.5$. By contrast, the simulation results for the concentration and configuration dependent voltages $V_{\boldsymbol{\sigma}}(x)$ shown in Fig. 11, together with Eqs. (4) and (6), indicate that the intercalation voltage for $\mathrm{Li}_{2+x}\mathrm{SnO}_3$ is predicted to be an *increasing* function of x.

Some details of this apparent descrepancy between the simulation results and experiment are as follows. For $\mathrm{Li}_{2+x}\mathrm{SnO}_3$ the limits of x for the voltage calculations were restricted to $0 \leq x \leq 0.5$. This was done because the break down of the lattice makes the voltage approximation less applicable due to increasing entropy and that as the system becomes disordered the configurational space becomes much larger. Even for the $0 \leq x \leq 0.5$ range, the lattice of interstitials can be described as metastable, so that an analytic cluster expansion[36] such as given in Eq. (9), is not well defined for $\mathrm{Li}_{2+x}\mathrm{SnO}_3$. For the calculated range of $0 \leq x \leq 0.5$ seen in Fig. 11, the results must be analyzed qualitatively keeping in mind that results higher in voltage for a particular x are more probable. Estimating the concentration and configuration averaged voltage from $V_{\boldsymbol{\sigma}}(x)$ given in Fig. 11 shows that the simulations predict a voltage which increases with x. For $0 \leq x \leq 0.5$, the voltage can be estimated as roughly 0.1 V $\lesssim V_{avg}(x) \lesssim 0.6$ V. It is notable that at the low concentration of $x = 0.0625$, the voltage is predicted to be ~ 0.9 V below that of experiment. In order to thoroughly study this particular concentration, 22 calculations were performed with a variety of supercells($1 \times 1 \times 4$, $2 \times 2 \times 1$, $2 \times 1 \times 2$, $4 \times 2 \times 1$). This was done to qualitatively study the Li-Li interactions on the interstitial lattice. Pair interactions were throughly studied, a sample of short to mid range three site interactions, some close ranged four site, and the possibility of staging into the layers. The results suggest it is unlikely that the large gap with experiment, at this particular $x = 0.0625$ concentration, can be explained by simply not having sampled the right configurations. The special result $V_{\boldsymbol{\sigma}}(x = 0.25) = 0.53$
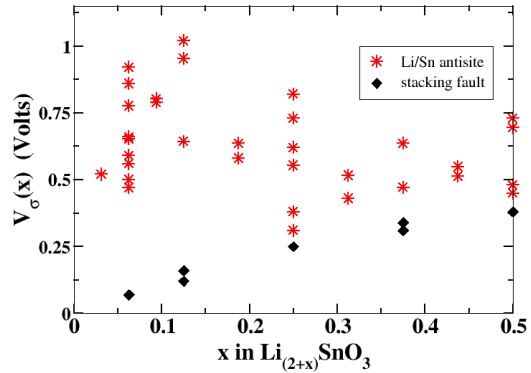

FIG. 12. (Color online) Sampling of $V_{\boldsymbol{\sigma}}(x)$ calculated with Eq. (8) for $\mathrm{Li}_{2+x}\mathrm{SnO}_3$ with antisite and stacking fault defects. Red stars represent results in the presence of Li/Sn antisite defects. Black diamonds represent results in the presence of stacking faults.

V was a configuration of four favorable pairs of Li interstitials identified while studying the $x = 0.0625$ case, dispersed uniformly in a $2 \times 2 \times 1$ supercell. The converged configuration retained the Li pair structure, but the resulting voltage cannot be explained by the the Li pair interactions found at $x = 0.0625$. This illustrates the concentration and configuration dependence of the voltage for this system.

In an effort to understand the discrepancy between the calculated voltage and experimental voltage for $\mathrm{Li}_{2+x}\mathrm{SnO}_3$, crude modeling of defects and their effect on voltage was done. The defects accounted for were antisite defects and stacking faults, both studied in the literature.[31,32] A brief study of the formation energy of Sn/Li antisite defects were calculated for a particular Sn(4e) site, in a $2 \times 1 \times 1$ supercell, swapped with its nearest 8f, 4d, or 4e lithium host lattice sites. Using Eq. (3) the formation energies for the Sn(4e)-Li(8f,4d,4e) antisite defects were calculated to be 2.3, 1.6, and 1.8 eV respectively. The Sn(4e)/Li(4d) was found to have the lowest formation energy and choosen for the model. This Sn(4e) site was equivalent to the (0.00,0.749,0.25) tin site listed in Appendix A. For a stacking fault a $2 \times 1 \times 1$ supercell was used with uppper most(along c-axis) $[\mathrm{Li}_{\frac{1}{3}}\mathrm{Sn}_{\frac{2}{3}}\mathrm{O}_2]$ plane shifted by the $[\frac{1}{2}, \frac{1}{6}, 0]$ suggested by Tarakina *et al.*[31] as the most probable with a 40% likelihood. Our simulation is a coarse approximation with 50% stacking faults imposed on every other $[\mathrm{Li}_{\frac{1}{3}}\mathrm{Sn}_{\frac{2}{3}}\mathrm{O}_2]$ plane. Using Eq.(3) the formation energy of this configuration is 0.01eV. Figure 12 shows a sampling of $V_{\boldsymbol{\sigma}}(x)$ for both of the defective structures. It is shown in these results that Sn/Li antisite defects can have a large impact on the voltage and greatly improves correspondence with experiment. The stacking fault results show very similar results to the voltage profiles of the simulations without stacking faults shown in Fig. 11.
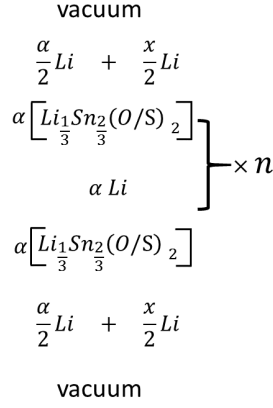
FIG. 13. Schematic diagram of surface geometries for $Li_{2+x}Sn(O/S)_3$ slabs in vacuum. Here x represents the excess lithium per formula unit and is assumed to be distributed equally on the two surfaces. The variable n determines the thickness of the slab. The normalizing factor $\alpha = \frac{3}{2(n+1)}$ is introduced so that the diagram corresponds to one unit of $Li_{2+x}Sn(O/S)_3$.

VI. SURFACES AND INTERFACES WITH LITHIUM

The purpose of studying surfaces and interfaces for Li_2SnO_3 and Li_2SnS_3 is to explore their interaction with lithium at the surface. Transmission electron microscopy images of Li_2SnO_3 reported by Wang et $al.$[10] show nano-flakes with their exposed surface in the a-b plane. Motivated by this observation, only surfaces and interfaces in the a-b plane were studied.

A. Surface simulations

Surface simulations were performed using the the slab geometry shown in Fig. 13. The supercells were simulated using fixed lattice constants based on the 1×1 cell in the a-b plane using the optimized a and b lattice constants and a slab thickness determined by $n = 4$ as defined in Fig. 13, corresponding to 20 formula units of $Li_{2+x}Sn(O/S)_3$. The vacuum distance separating the periodic slabs was chosen to be 15Å for $Li_{2+x}SnO_3$ and 18.7Å for $Li_{2+x}SnS_3$.

A convenient measure of surface stability is the surface energy which can be defined according to

$$\gamma = \frac{E_{slab} - NE_{bulk} - xE_{\text{Li}}}{2\mathcal{A}} \quad (11)$$

Here E_{slab} and E_{bulk} denote the total electronic energies of the slab and of the bulk $Li_2Sn(O/S)_3$, respectively. N is the number of formula units in the slab and E_{Li} denotes the total energy per atom of bcc Li. $\mathcal{A}$ denotes the area of a single surface plane in the simulation cell.

For this surface geometry, the stoichiometric surface ($x = 0$) is missing half of its Li sites. For convenience,

the simulations assumed that the missing sites were distributed evenly over the two simulation surfaces. For the chosen supercell, simulations with 2, 4, and 6 extra Li atoms correspond to $x = 0.1, 0.2$, and 0.3, respectively. Figure 14 shows the results for the surface energies of Li_2SnS_3 and Li_2SnO_3. This figure shows both materials tend to lower their surface energy when absorbing lithium, which is indicative of a favorable process.
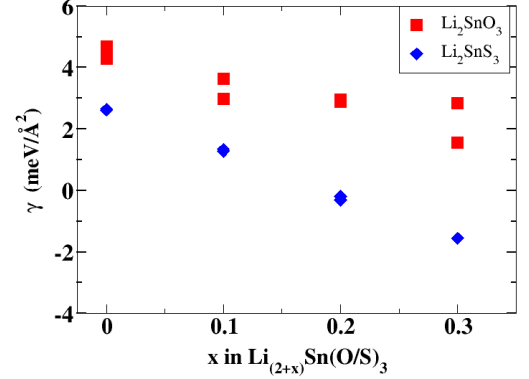

FIG. 14. (Color online) Surface energies as a function of x as defined in Eq. (11 with $Li_{2+x}SnO_3$ shown as red squares and $Li_{2+x}SnS_3$ with blue diamonds. For all concentrations except $Li_{2.3}SnS_3$, two or more configurations were modeled.
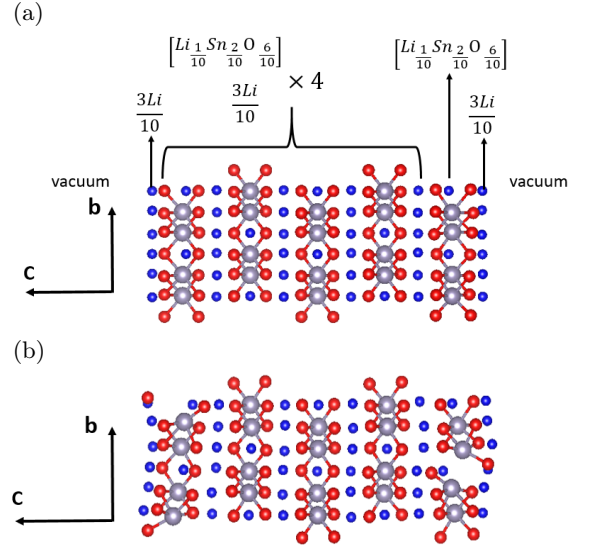

FIG. 15. Optimized surfaces for $Li_{2+0.3}SnO_3$ with different initial positions. In (a), the initial surface Li positions were the ideal bulk lattice sites. In (b), random noise added to the surface lithium sites.

Multiple meta-stable configurations were found for excess Li concentrations $x > 0$ as indicated in Fig. 14. An interesting example is shown in Fig. 15 which shows two configurations of $Li_{2+0.3}SnO_3$. The configuration shown

in Fig. 15(a) was optimized from the ideal bulk positions of the surface Li sites. The configuration in Fig. 15(b) was optimized from randomized positions of the surface Li sites and has a lower value of γ by 1 meV/$\mathring{A}^2$. The corresponding partial densities of states plots for these two cases are shown in Fig. 16. These results show that the metastable ordered configuration has a partial density of states much like that of the bulk lattice with the Fermi level raised to within the conduction band due to the excess Li atoms at the surface. The relaxed configuration shows new states within the bulk band gap which are due to broken Sn-O bonds.
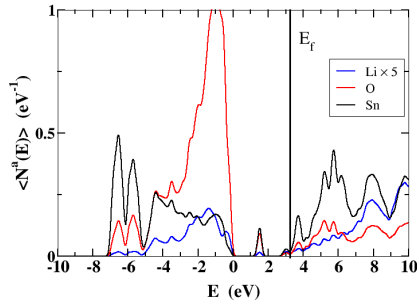
(a)
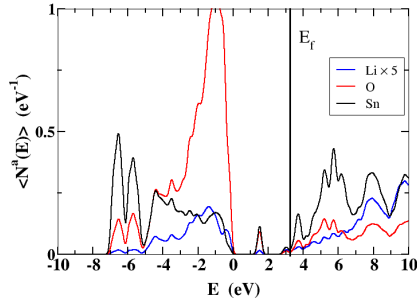
(b)

FIG. 16. (Color online) Partial densities of states for (a) ordered and (b) disordered $Li_{2+0.3}SnO_3$ surfaces. In each plot, the Li contribution has been scaled by 5.

Less variation in the surface geometries and energies were found for the $Li_{2+x}SnS_3$ simulations. The partial density of states are shown in Fig. 17. In this case, the density of states is similar to that of the bulk with the Fermi level located within the Sn-S conduction band due to the excess surface Li atoms. The shift in the energies of the conduction band states is localized to the surface layer Sn $5s$ states.

B. Interface simulations

To further explore the interaction of these materials with lithium interface calculations where done with bulk lithium using slab geometry. The converged results from
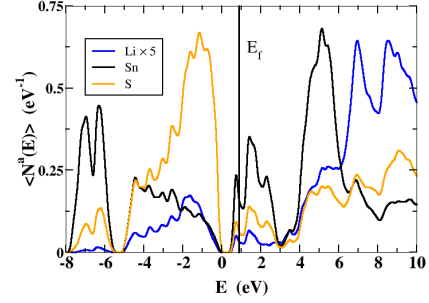

FIG. 17. (Color online) Partial densities of states for a $Li_{2+0.3}SnS_3$ surface. In this plot, the Li contribution has been scaled by 5.

the $x = 0.3$ surface calculations, with lithium left in their native positions from the layers, were used as the starting point for these simulations. The vacuum of these relaxed surface calculations were filled with 30 Li atoms distributed uniformly and at a density that is approximately that of bulk lithium. These structures were optimized with fixed lattice parameters in the layer planes while the supercell dimension perpendicular to the layers was allowed to vary.

Figure 18 shows the optimized geometry for the ideal Li_2SnO_3/Li interface. In this case, the converged geometry of the lithium slab resembles that of bcc lithium, skewed by the interface boundary. While this ideal interface has been found, it is meta-stable relative to the formation of Li_2O. For example, displacing one of the surface O sites into the lithium slab generally results in a lower energy structure (by 1.5 eV in one example) with broken Sn-O bonds.

Figure 19 shows the optimized geometry for the Li_2SnS_3/Li interface, showing that Li_2SnS_3 undergoes a decomposition at the surface. In order to examine the Li_2SnS_3/Li in greater detail, partial densities of states from four different sections of the calculation slab were analyzed as shown in Fig. 19. The top section represents pure metallic Li. The second section resembles Li_2S, while the third section shows SnS_x with many Sn-S bonds broken. The central layer of the slab represents bulk Li_2SnS_3.
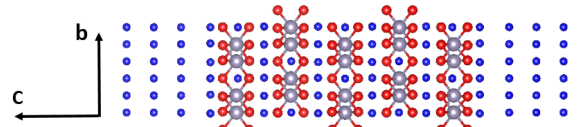

FIG. 18. (Color on line.) Ball and stick model of the optimized ideal interface of Li_2SnO_3/Li. Li, Sn, and O are indicated with blue, grey, and red balls, respectively.
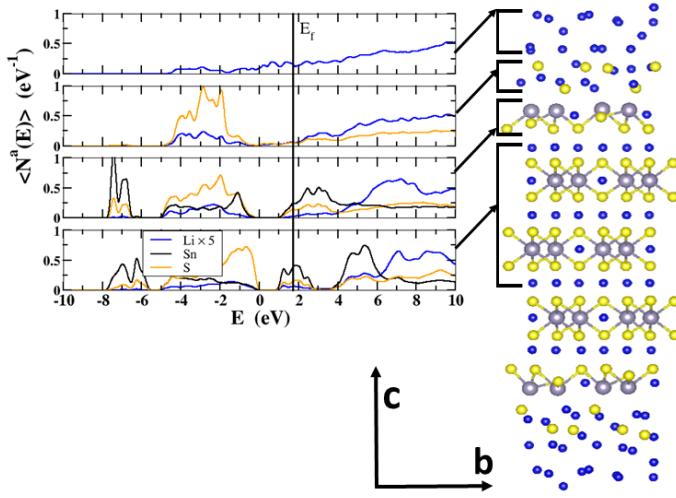
FIG. 19. (Color online) Partial densities of states of regions of the optimized interface of Li_2SnS_3/Li (with Li contributions scaled by factor of 5). The corresponding ball and stick model of the optimized geometry is shown on the right of the diagram with Li, Sn, and S indicated with blue, grey, and yellow balls.

VII. DISCUSSION AND CONCLUSIONS

The results of these simulations show that, despite the fact that the porous layered calcogenide materials Li_2SnO_3 and Li_2SnS_3 both have the same crystal structure based on the space group C2/c, they have very different responses to excess Li. An important component of the explanation is the qualitative differences in the band structures of the two materials. Li_2SnS_3 has an unoccupied conduction band formed from Sn 5s and S 3p states[4] located 1 eV above the valence band. The simulations for $Li_{2+x}SnS_3$ show that these bands readily accomodate the excess electrons from lithiation. Figure 9 shows isosurface plots for electrons within this band for particular configurations of the lithiated material for $x = 0.5$ and $x = 1$, illustrating the antibonding Sn 5s and S 3p states. A consequence of this lithiation mechanism is the predicted constant voltage versus Li concentration x as shown in Fig. 10. By contrast, in Li_2SnO_3 the corresponding bands for Sn 5s and O 2p states lie much higher in energy. The simulation show that the lithiation process is still energetically favorable, but in order to accommodate the excess electrons, new localized states are formed within the band gap of the material. The simulations show that these states are typically associated with broken Sn-O bonds such as shown in Fig. 7.

Calculations of the voltage versus lithium concentration for $Li_{2+x}SnO_3$ shown in Figs. 11 and 12 demonstrate that Li/Sn antisite defects can have a significant impact on the voltage profiles. The results suggest that Li/Sn antisite defects are present in the experimental samples presented in the literature.[8–10] Preliminary computational results for Li/Sn antisite defects in $Li_{2+x}SnS_3$ suggest their effects on the voltage profiles are small. Our calculations for defect free $Li_{2+x}SnS_3$ predict a constant voltage versus lithium concentration, which has not yet been confirmed experimentally. Assuming that the lithiation proceeds to the concentration of $x = 1$ without interference from possible competing reactions, the theoretical capacity is estimated to be 117 mAh/g.

For both materials, the most efficient ion migration processes were shown to involve the interstitial sites in interstitiacy mechanisms with net migration perpendicular to the porous layers as shown in Fig. 4, finding $E_m = 0.14$ eV and $E_m = 0.22$ eV for pristine Li_2SnO_3 and Li_2SnS_3, respectively. Recently, nuclear magnetic resonance experiments on Li_2SnO_3 have detected signals corresponding to the three unique Li sites, finding evidence for the predominant diffusion pathway to occur perpendicular to the a-b layer planes.[37] This is in qualitative agreement with the calculations, although the analysis of the experiments did not involve consideration of interstitial sites. Comparing the calculated results for E_m with activation energies E_a extracted from impedance measurements, suggests that the bottleneck for ion migration in the pristine materials is the formation of vacancy-interstitial pairs. For lithiated $Li_{2+x}SnS_3$, we expect there to be a sizeable population of interstitial Li ions so that their migration should be dominated by E_m. Further computational and experimental investigations are needed to verify whether or not the activation energy of lithiated $Li_{2+x}SnS_3$ has the expected small value of $E_a \approx E_m = 0.2$ eV.

Simulations of surfaces and interfaces of these materials suggest that it is energetically favorable to add a small amount of excess Li at the surface, but the surfaces seem to be reactive when interfaced with Li metal. While a meta-stable interface of Li_2SnO_3/Li was found, displacing surface O atoms was found to lower the energy of the model interface. The modeled interface of Li_2SnS_3/Li found the likely formation of Li_2S and the breaking of Sn-S bonds. These simulations are very sensitive to the initial model geometries. Additional simulations would be needed to go beyond the qualitative observation that the interfaces are reactive with respect to Li metal.

Appendix A: Structural details

For completeness, the unique positions of the atoms within the conventional cells of Li_2SnO_3 and Li_2SnS_3 are listed in Table IV. The calculated fractional coordinates agree well with the experimental results. Additionally, after shifting the origin of the coordinate systems, the two materials are shown to have very similar fractional coordinates.

TABLE IV. Fractional coordinates (x, y, z) of unique atoms in the conventional unit cells of Li_2SnO_3 and Li_2SnS_3 compared with experimental measurements reported by Refs. 2 and 4 respectively. The "site" column lists the site multiplicity and Wyckoff label. In order to more easily compare the two structures, the crystal origin chosen by Ref. 4 for Li_2SnS_3 was shifted by $(0, \frac{1}{2}, \frac{1}{2})$.

	Atom	Site	Comp.	Exp.
Li_2SnO_3	Li	8f	(0.232, 0.077,-0.001)	(0.239, 0.078,-0.001)
	Li	4e	(0.000, 0.085, 0.250)	(0.000, 0.083, 0.250)
	Li	4d	(0.250, 0.250, 0.500)	(0.250, 0.250, 0.500)
	Sn	4e	(0.000, 0.417, 0.250)	(0.000, 0.417, 0.250)
	Sn	4e	(0.000, 0.749, 0.250)	(0.000, 0.751, 0.250)
	O	8f	(0.134, 0.258, 0.131)	(0.134, 0.260, 0.133)
	O	8f	(0.114, 0.583, 0.131)	(0.110, 0.584, 0.134)
	O	8f	(0.133, 0.909, 0.129)	(0.135, 0.909, 0.133)
Li_2SnS_3	Li	8f	(0.256, 0.085, 0.000)	(0.253, 0.084, 0.000)
	Li	4e	(0.000, 0.083, 0.250)	(0.000, 0.083, 0.250)
	Li	4d	(0.250, 0.250, 0.500)	(0.250, 0.250, 0.500)
	Sn	4e	(0.000, 0.417, 0.250)	(0.000, 0.417, 0.250)
	Sn	4e	(0.000, 0.750, 0.250)	(0.000, 0.750, 0.250)
	S	8f	(0.132, 0.255, 0.128)	(0.136, 0.258, 0.131)
	S	8f	(0.115, 0.583, 0.127)	(0.112, 0.583, 0.131)
	S	8f	(0.132, 0.911, 0.126)	(0.135, 0.908, 0.127)

Appendix B: Lithiation effects on cell dimension

The results presented here detail the lithiation studies discussed in Sec. V A. Figures 20, 21 and 22 show changes in volume and lattice parameters calculated from a random sampling of configurations in $2 \times 1 \times 1$ supercells. For $Li_{2+x}SnO_3$, two or more configurations were sampled for $x > 0.0625$. For $x = 1$, although there is only one ideal configuration for the interstitial lattice, the system is highly meta-stable such that a small displacement in the initial ideal configuration results in significantly different optimized lattice parameters. For $Li_{2+x}SnS_3$, two configurations were sampled for $0.0625 < x < 1$. For this system, the results for each concentration are relatively insensitive to the initial configurations of interstitial placements. The points on the graphs represent simple averages and the error bars represent the standard deviations of the mean from the those averages.
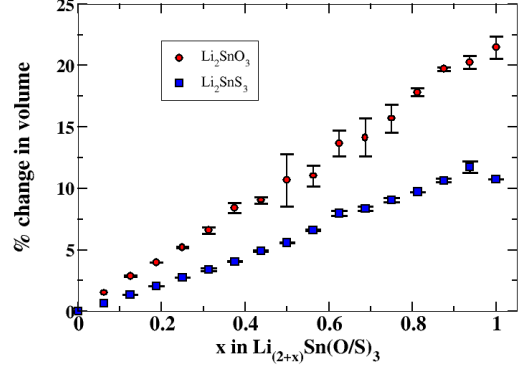
FIG. 20. (Color online) Percent change in volume for $Li_{2+x}SnO_3$ (red circles) and $Li_{2+x}SnS_3$ (blue squares). Error bars are the standard deviation of the mean.
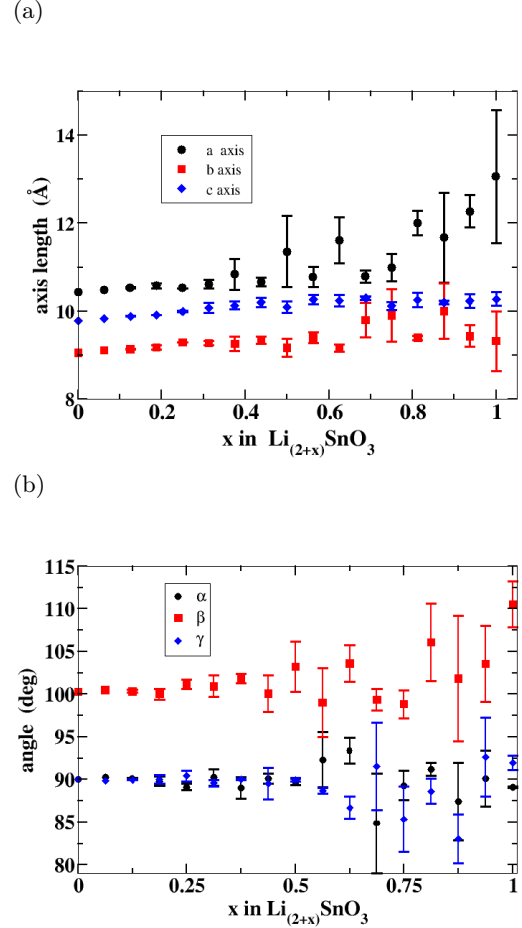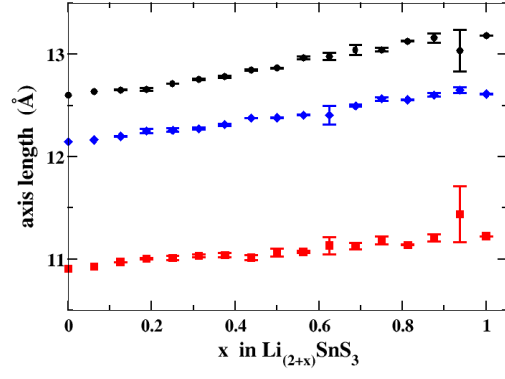
(a)

(b)

FIG. 21. (Color online) Average cell dimensions (a) and angles (b) for $Li_{2+x}SnO_3$. Error bars are the standard deviation of the mean.
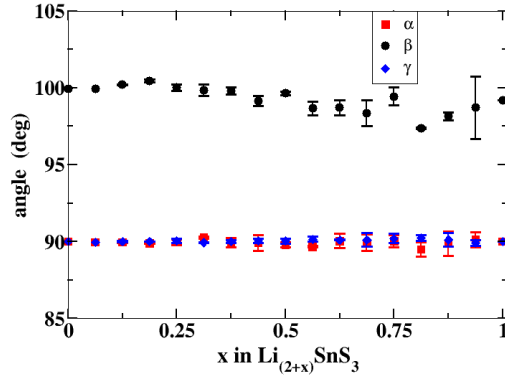
(a)

(b)

FIG. 22. (Color online) Average cell dimensions (a) and angles (b) for $Li_{2+x}SnS_3$. Error bars are the standard deviation of the mean.

* email:natalie@wfu.edu

[1] R. M. Hazen and L. W. Finger, American Mineralogist **63**, 289 (1978).

[2] G. Kreuzburg, F. Stewner, and R. Hoppe, Zeitschrift für Anorganische und Allgemeine Chemie **379**, 242 (1971).

[3] A. Kuhn, T. Holzmann, J. Nuss, and B. V. Lotsch, J. Mater. Chem. A **2**, 6100 (2014).

[4] J. A. Brant, D. M. Massi, N. A. W. Holzwarth, J. H. Mac-Neil, A. P. Douvalis, T. Bakas, S. W. Martin, M. D. Gross, and J. A. Aitken, Chemistry of Materials **27**, 189 (2015).

[5] Y.-C. Chen, M. Huo, Y. Liu, T. Chen, C.-C. Leng, Q. Li, Z.-L. Sun, and L.-J. Song, Chinese Physics Letters **32**, 017102 (2015).

[6] G. Vitins, G. Kizane, A. Lusis, and J. Tiliks, Journal of Solid State Electrochemistry **6**, 311 (2002).

[7] L. Teo, M. Buraidah, A. Nor, and S. Majid, Ionics **18**, 655 (2012).

[8] I. A. Courtney and J. R. Dahn, Journal of The Electrochemical Society **144**, 2045 (1997).

[9] D. Zhang, S. Zhang, Y. Jin, T. Yi, S. Xie, and C. Chen, Journal of Alloys and Compounds **415**, 229 (2006).

[10] Q. Wang, Y. Huang, Y. Zhao, W. Zhang, and Y. Wang, Surface and Interface Analysis **45**, 1297 (2013).

[11] T.-J. Kim, C. Kim, D. Son, M. Choi, and B. Park, Journal of Power Sources **167**, 529 (2007).

[12] A. Pedersen and M. Luisier, ACS Applied Materials & Interfaces **6**, 22257 (2014).

[13] P. Hohenberg and W. Kohn, Physical Review **136**, B864 (1964).

[14] W. Kohn and L. J. Sham, Physical Review **140**, A1133 (1965).

[15] P. E. Blöchl, Phys. Rev. B **50**, 17953 (1994).

[16] N. A. W. Holzwarth, A. R. Tackett, and G. E. Matthews, Computer Physics Communications **135**, 329 (2001), available from the website `http://pwpaw.wfu.edu`.

[17] P. Giannozzi, S. Baroni, N. Bonini, M. Calandra, R. Car, C. Cavazzoni, D. Ceresoli, G. L. Chiarotti, M. Cococcioni, I. Dabo, A. D. Corso, S. de Gironcoli, S. Fabris, G. Fratesi, R. Gebauer, U. Gerstmann, C. Gougoussis, A. Kokalj, M. Lazzeri, L. Martin-Samos, N. Marzari, F. Mauri, R. Mazzarello, S. Paolini, A. Pasquarello, L. Paulatto, C. Sbraccia, S. Scandolo, G. Sclauzero, A. P. Seitsonen, A. Smogunov, P. Umari, and R. M. Wentzcovitch, J. Phys.: Condens. Matter **21**, 394402 (19pp) (2009), available from the website `http://www.quantum-espresso.org`.

[18] J. P. Perdew and Y. Wang, Phys. Rev. B **45**, 13244 (1992).

[19] The choice of LDA functional was made based on previous investigations[23,24,38–41] of similar materials which showed that provided that the lattice constants are scaled by a correction factor of 1.02, the simulations are in good agreement with experiment, especially lattice vibrational frequencies and heats of formation.

[20] H. Jónsson, G. Mills, and K. W. Jacobsen, in *Classical and Quantum Dynamics in Condensed Phase Simulations*, edited by B. J. Berne, G. Ciccotti, and D. F. Coker (World Scientific, Singapore, 1998) pp. 385–404.

[21] G. Henkelman, B. P. Uberuaga, and H. Jónsson, J. Comp. Phys. **113**, 9901 (2000).

[22] G. Henkelman and H. Jónsson, J. Comp. Phys. **113**, 9978 (2000).

[23] N. D. Lepley, N. A. W. Holzwarth, and Y. A. Du, Phys. Rev. B **88**, 104103 (11 pp) (2013).

[24] Z. D. Hood, C. Kates, M. Kirkham, S. Adhikari, C. Liang, and N. A. W. Holzwarth, Solid State Ionics **284**, 61 (2015).

[25] A. R. Tackett, N. A. W. Holzwarth, and G. E. Matthews, Computer Physics Communications **135**, 348 (2001), available from the website `http://pwpaw.wfu.edu`.

[26] OpenDX – The Open Source Software Project Based on IBM's Visualization Data Explorer – is available from the web site `http://www.opendx.org`.

[27] A. Kokalj, Journal of Molecular Graphics and Modelling **17**, 176 (1999), Code available at the website `http://www.xcrysden.org`.

[28] A. Kokalj, Computational Materials Science **28**, 155 (2003).

[29] K. Momma and F. Izumi, Applied Crystallography **44**, 1272 (2011), Code available from the website `http://jp-minerals.org/vesta/en/`.

[30] T. Hahn, ed., *International Tables for Crystallography, Volume A: Space-group symmetry, Fifth revised edition* (Kluwer, 2002) ISBN 0-7923-6590-9.

[31] N. V. Tarakina, T. A. Denisova, L. G. Maksimova, Y. V. Baklanova, A. P. Tyutyunnik, I. F. Berger, V. G. Zubkov, and G. Van Tendeloo, Zeitschrift fur Kristallographie Supplements **30**, 375 (2009).

[32] Z. Wang, Y. Ren, T. Ma, W. Zhuang, S. Lu, G. Xu, A. Abouimrane, K. Amine, and Z. Chen, RSC Adv. **6**, 31559 (2016).

[33] A. R. West, *Basic Solid State Chemistry, second edition* (John Wiley & Sons, LTD, 1999).

[34] W. Hayes and A. M. Stoneham, *Defects and Defect Processes in Nonmetallic Solids* (John Wiley and Sons, 1985).

[35] M. K. Aydinol, A. F. Kohan, G. Ceder, K. Cho, and J. Joannopoulos, Phys. Rev. B **56**, 1354 (1997).

[36] D. de Fontaine, in *Solid State Physics*, Vol. 47 (Academic Press, Inc., 1994) pp. 33–176.

[37] J. Langer, D. L. Smiley, A. D. Bain, G. R. Goward, and M. Wilkening, The Journal of Physical Chemistry C **120**, 3130 (2016).

[38] Y. A. Du and N. A. W. Holzwarth, Phys. Rev. B **76**, 174302 (14 pp) (2007).

[39] N. A. W. Holzwarth, N. D. Lepley, and Y. A. Du, Journal of Power Sources **196**, 6870 (2011).

[40] Y. A. Du and N. A. W. Holzwarth, Phys. Rev. B **81**, 184106 (15pp) (2010).

[41] K. Senevirathne, C. S. Day, M. D. Gross, A. Lachgar, and N. A. W. Holzwarth, Solid State Ionics **333**, 95 (2013).